Chinese Journal of Aeronautics, (2015),28(1): 44–56

Chinese Society of Aeronautics and Astronautics
& Beihang University

Chinese Journal of Aeronautics

cja@buaa.edu.cn
www.sciencedirect.com

Stationary flow fields prediction of variable physical domain based on proper orthogonal decomposition and kriging surrogate model

Qiu Yasong, Bai Junqiang *

School of Aeronautics, Northwestern Polytechnical University, Xi'an 710072, China

Received 18 February 2014; revised 23 March 2014; accepted 16 April 2014
Available online 26 December 2014

KEYWORDS

Compressible-viscous flows;
Kriging surrogate model;
Proper orthogonal decomposition;
Shock wave;
Variable physical domain

Abstract In this paper a new flow field prediction method which is independent of the governing equations, is developed to predict stationary flow fields of variable physical domain. Predicted flow fields come from linear superposition of selected basis modes generated by proper orthogonal decomposition (POD). Instead of traditional projection methods, kriging surrogate model is used to calculate the superposition coefficients through building approximate function relationships between profile geometry parameters of physical domain and these coefficients. In this context, the problem which troubles the traditional POD-projection method due to viscosity and compressibility has been avoided in the whole process. Moreover, there are no constraints for the inner product form, so two forms of simple ones are applied to improving computational efficiency and cope with variable physical domain problem. An iterative algorithm is developed to determine how many basis modes ranking front should be used in the prediction. Testing results prove the feasibility of this new method for subsonic flow field, but also prove that it is not proper for transonic flow field because of the poor predicted shock waves.

© 2015 Production and hosting by Elsevier Ltd. on behalf of CSAA & BUAA.

1. Introduction

For some systems governed by complex equations, a reduced order model (ROM) which approximates the high-fidelity (HF) models well with rather fewer states can be generated by some certain methods. So, developing efficient ROMs to improve computational efficiency is a hot issue in computational physics now. The combination of proper orthogonal decomposition (POD)[1–3] and projection methods (POD-projection) is such a research direction in the area of fluid dynamics. This strategy approximates the HF result by the linier superposition of some selected basis modes, and the coefficients of these selected basis modes are determined by solving ordinary differential equations (ODEs) generated from projecting the governing equations onto the selected basis modes.

In the past decades, many problems in fluid dynamics have got corresponding ROMs through POD-projection approach. Two projection methods for applying this strategy in problems governed by Euler equations are presented in Ref.[4] ROMs about aeroelasticity of airfoil[5,6] and turbine engine[7] have also

* Corresponding author. Tel.: +86 29 88492694.
E-mail address: junqiang@nwpu.edu.cn (J. Bai).

Peer review under responsibility of Editorial Committee of CJA.

ELSEVIER Production and hosting by Elsevier

http://dx.doi.org/10.1016/j.cja.2014.12.017
1000-9361 © 2015 Production and hosting by Elsevier Ltd. on behalf of CSAA & BUAA.

been derived. But all these applications above ignored the fluid viscosity. It is true that problems which concern viscosity could also be handled by this approach. For example, Ma and Karniadakis[8] investigated the stability and dynamics of three-dimensional limit-cycle states inflow past a circular cylinder using ROM generated by POD-projection strategy. Other similar literature includes laminar, transitional and turbulent flows simulation,[9–13] flow field calculation and control in chemical process[14] and free surface shallow water flows.[15] However, these problems all ignored the compressibility of fluid.

Not many researches have been conducted concerning the problems that concern compressible viscous flows by POD-projection strategy. Rowley et al.[16] got the ROM for compressible Navier–Stokes equations, but the flow must be isentropic. Bourguet et al.[17] extended the application to transonic flows around airfoil, which are governed by Navier–Stokes equations. While, the flow fields are constrained under constant viscosity assumption. It is worth noting that all the constraints above come from the projection process. For realizing the projection process, the governing equations should be modified into some forms to lead quadratic fluxes, and the inner product should make dimensional sense.[16] Besides compressibility and viscosity, variable physical domain, which means that the domain occupied by the flow field is variable, also causes troubles for the application of POD-projection, because the projection process requires a fixed physical domain in principle. Of course, this problem has been solved in some cases. For the physical domain discretized by structured meshes, index-based POD[6,18,19] could be used to eliminate this problem. In addition, Hadamard formulation could also be used to cope with small deformations of physical domain in POD-projection process.[17]

All the drawbacks presented above can be summarized as the so-called intrusive feature: starting from an existing computational code, additional derivations and programming efforts required to develop a ROM.[20] Bui-Thanh et al.[21] combined POD with cubic spline interpolation to predict inviscid flow field of fixed airfoil when a single parameter, such as the angle of attack or inflow Mach number, is changed. This method gets over the intrusive feature, but can just treat single parameter problems, and the physical domain should still be fixed because of the constraint from inner product. Qiu et al.[22] presented a new strategy to predict flow field by the combination of surrogate model and POD. Compared with the combination of cubic spline interpolation and POD, multi-parameters problems could be handled easily by this method.

Following the work presented in Ref.[22], this paper is devoted to develop a simpler and more precise ROM method for stationary flow field prediction. For that, the combination of POD and kirging surrogate model[23] is used to build ROM system. Two simple forms of index-based inner product are applied into the POD process, which improve the computational efficiency and make the physical domain variation problems very easy. Meanwhile, an efficient algorithm, which is used to determine how many basis modes ranking front should be used, is proposed in this paper.

Brief introductions of POD and kriging surrogate model are presented in Sections 2 and 3 respectively. Section 4.1 introduces flow field prediction method based on the combination of POD and kriging surrogate model in detail. The algorithm used to determine the basis modes number is presented out in Section 4.2. Following that, the applying of different forms of inner product is discussed. Section 5 presents two sets of prediction results and the corresponding analysis under different flow conditions. A brief summary is concluded in Section 6.

2. Proper orthogonal decomposition and POD-projection system

To use POD method, the data set should be pre-treated. Normally, there are two forms,[24] covariance form and correlation form, to pre-treat the data set from the perspective of statistics. The first one is the most common method, and the second method is more suited to data with mixed units and significant magnitude difference. Since the results generated by the CFD code in present work are dimensionless, the covariance method is adopted here.

Let $\{\boldsymbol{U}^{(i)}(x) : 1 \le i \le N, x \in \Omega\}$ represent a set of N sample flow fields (called snapshots commonly), Ω is the physical domain of flow field, and we deem each snapshot as a vector. With covariance method, each snapshot should be rewritten in the form of $\boldsymbol{U}^{(i)}(x) = \tilde{\boldsymbol{U}}^{(i)}(x) + \overline{\boldsymbol{U}}(x)$, and $\overline{\boldsymbol{U}}(x)$ is the average of all snapshots. Then the vector set $\{\tilde{\boldsymbol{U}}^{(i)}(x) : 1 \le i \le N, x \in \Omega\}$ can span a linear space $\boldsymbol{\Psi}$. POD method is used to decompose space $\boldsymbol{\Psi}$ into a set of orthogonal basis $\{\boldsymbol{\Phi}^{(i)}(x) : 1 \le i \le N, x \in \Omega\}$ (called basis modes) which has the maximum mean square projection on all snapshots. This leads to such a constrained maximization problem:

$$\begin{aligned} &\max \ \frac{1}{N}\sum_{i=1}^{N}\left|\left(\tilde{\boldsymbol{U}}^{(i)}, \boldsymbol{\Phi}\right)\right|^2 \\ &\text{s.t.} \quad (\boldsymbol{\Phi}, \boldsymbol{\Phi}) = 1 \end{aligned} \tag{1}$$

where $(\cdot\,,\,\cdot)$ and $|\cdot|$ are inner product operation and norm defined on $\boldsymbol{L}^2$ (square integrable space, SIS) respectively. Since $\{\boldsymbol{\Phi}^{(i)}(x) : 1 \le i \le N, x \in \Omega\}$ is a set of orthogonal basis of space $\boldsymbol{\Psi}$ which is spanned by $\{\tilde{\boldsymbol{U}}^{(i)}(x) : 1 \le i \le N, x \in \Omega\}$, then each basis mode $\boldsymbol{\Phi}$ can be represented by the linear superposition of $\tilde{\boldsymbol{U}}^{(i)}(x)$ as

$$\boldsymbol{\Phi} = \sum_{i=1}^{N} a^{(i)}\tilde{\boldsymbol{U}}^{(i)} \tag{2}$$

If all the coefficients $a^{(i)}$ are solved out, then the basis modes are known. The so-called Rayleigh-Rita method[25] could be used to solve this problem above. Literature[14] presents the process for the most common solution. First it defines a core function

$$\boldsymbol{K}(x, x') = \frac{1}{N}\sum_{i=1}^{N}\tilde{\boldsymbol{U}}^{(i)}(x)\tilde{\boldsymbol{U}}^{(i)}(x') \tag{3}$$

and an operator

$$\boldsymbol{R\Phi} = \int_{\Omega}\boldsymbol{K}(x, x')\boldsymbol{\Phi}(x')\mathrm{d}x' \tag{4}$$

where $\boldsymbol{R} : \boldsymbol{L}^2(\Omega) \to \boldsymbol{L}^2(\Omega)$. Inner product operation between $\boldsymbol{R\Phi}$ and $\boldsymbol{\Phi}$ leads

$$(\boldsymbol{R\Phi}, \boldsymbol{\Phi}) = \int_{\Omega}\boldsymbol{R\Phi}(x)\boldsymbol{\Phi}(x)\mathrm{d}x = \frac{1}{N}\sum_{i=1}^{N}\left|\left(\tilde{\boldsymbol{U}}^{(i)}, \boldsymbol{\Phi}\right)\right| \tag{5}$$

The right side of this equation is equal to the target of Eq. (1). So, the maximization problem then transforms into finding the maximum eigenvalue of

$$\begin{aligned} &\boldsymbol{R}\boldsymbol{\Phi} = \lambda\boldsymbol{\Phi} \\ &\text{s.t.} \quad (\boldsymbol{\Phi}, \boldsymbol{\Phi}) = 1 \end{aligned} \tag{6}$$

The expression above in detail is

$$\begin{aligned} &\int_{\Omega} \boldsymbol{K}(x, x')\boldsymbol{\Phi}(x')\mathrm{d}x' = \lambda\boldsymbol{\Phi} \\ &\text{s.t.} \quad (\boldsymbol{\Phi}, \boldsymbol{\Phi}) = 1 \end{aligned} \tag{7}$$

Substituting Eqs. (2) and (3) into the equation above, we will obtain

$$\begin{aligned} &\sum_{i=1}^{N}\left[\sum_{k=1}^{N}\left(\frac{1}{N}\int_{\Omega}\tilde{\boldsymbol{U}}^{(i)}(x')\tilde{\boldsymbol{U}}^{(k)}(x')\mathrm{d}x'\right)a^{(k)}\right]\tilde{\boldsymbol{U}}^{(i)}(x) \\ &= \sum_{i=1}^{N}\lambda a^{(i)}\tilde{\boldsymbol{U}}^{(i)}(x) \end{aligned} \tag{8}$$

which can be rewritten as another eigenvalue problem as

$$\boldsymbol{C}\boldsymbol{V} = \lambda\boldsymbol{V} \tag{9}$$

where $\boldsymbol{C}$ is a $N \times N$ matrix with $\boldsymbol{C}_{ij} = (\tilde{\boldsymbol{U}}^{(i)}, \tilde{\boldsymbol{U}}^{(j)})/N$, and $\boldsymbol{V}$ is the eigenvector corresponding to eigenvalue λ. So $\boldsymbol{C}$ is a non-negative symmetric matrix, and it has a complete set of orthogonal eigenvectors

$$\boldsymbol{V}^{(i)} = \left[a_1^{(i)} a_2^{(i)} \cdots a_N^{(i)}\right]^{\mathrm{T}}, \quad 1 \le i \le N \tag{10}$$

Then the coefficients for the ith basis mode in Eq. (2) are the elements of the ith eigenvector of matrix $\boldsymbol{C}$, namely

$$\boldsymbol{\Phi}^{(i)} = \sum_{j=1}^{N} a_j^{(i)}\tilde{\boldsymbol{U}}^{(j)} \tag{11}$$

Usually, all the N basis modes are sequenced in descending order of their corresponding eigenvalues, because those basis modes corresponding to bigger eigenvalues contain more snapshot characteristics than others. The criteria that used to measure the amount of snapshots characteristics contained in the first M $(1 \le M \le N)$ basis modes is so-called energy,[2] which is defined as

$$E_{\mathrm{n}M} = \sum_{i=1}^{M}\lambda^{(i)} \Big/ \sum_{j=1}^{N}\lambda^{(j)} \tag{12}$$

In most cases, just the first few basis modes would contain most ($\ge 99\%$) energy of the snapshot set. So, each snapshot can be approximated by the linear superposition of these modes

$$\boldsymbol{U}^{(i)}(x) \approx \sum_{j=1}^{P} b^{(j)}\boldsymbol{\Phi}^{(j)}(x) + \overline{\boldsymbol{U}}(x), \ (E_{\mathrm{n}P} \ge 99\%, \quad P << N) \tag{13}$$

This is the famous 99% energy criteria proposed by Sirovich.[2] The coefficients $b^{(j)}$ can be solved out by least square method, which leads to such equations

$$\boldsymbol{M}\boldsymbol{b} = \boldsymbol{f} \tag{14}$$

where $\boldsymbol{M}_{jk} = (\boldsymbol{\Phi}^{(k)}(x), \boldsymbol{\Phi}^{(j)}(x))\big|_{k,j=1}^{P}$, $\boldsymbol{b} = [b^{(1)}, b^{(2)}, \cdots, b^{(P)}]^{\mathrm{T}}$ and $\boldsymbol{f}_j = (\tilde{\boldsymbol{U}}^{(i)}(x), \boldsymbol{\Phi}^{(j)}(x))\big|_{j=1}^{P}$. Since the basis modes is a set of orthonormal basis, $b^{(j)}$ can be solved directly from

$$b^{(j)} = \left(\tilde{\boldsymbol{U}}^{(i)}(x), \boldsymbol{\Phi}^{(j)}(x)\right)\big|_{j=1}^{P} \tag{15}$$

Any flow field $\boldsymbol{U}(x)$, which is not included in the snapshot set and unknown in prior, could also be approximated by the linear superposition of the selected modes, namely

$$\boldsymbol{U}(x) \approx \sum_{j=1}^{P} b^{(j)}\boldsymbol{\Phi}^{(j)}(x) + \overline{\boldsymbol{U}}(x), \quad P << N \tag{16}$$

Since $\boldsymbol{U}(x)$ is unknown in prior, the coefficients $b^{(j)}$ here could not be found out by solving Eq. (15). Instead, projecting the governing equations onto selected basis modes is used to solve them out. Generally, projection means to do inner product operation between selected basis modes and the governing equations. It will lead to a set of simple ODEs which could be solved easily. But, as mentioned in Section 1, the projection process itself is not easy when the governing equations are very complex.

3. Kriging surrogate model

Let $\{\boldsymbol{X}^{(i)} : 1 \le i \le N\}$ represent a set of N input parameters vectors from samples, for each vector, there are z elements, namely $\boldsymbol{X}^{(i)} = \left[x_1^{(i)}, x_2^{(i)}, \cdots, x_z^{(i)}\right]^{\mathrm{T}}$. The sample output parameters vector is $\boldsymbol{Y} = [y_1, y_2, \ldots, y_N]^{\mathrm{T}}$, here $y_i (1 \le i \le N)$ represents the corresponding output scalar values of $\boldsymbol{X}^{(i)}$ $(1 \le i \le N)$. $\boldsymbol{Y}$ could be generated by high fidelity simulations or experiments. Now we want to use these samples to predict the output value when input vector $\boldsymbol{X}$ is beyond the samples. Kirging surrogate model presumes the real function relationship between the input vector and output value as

$$y(\boldsymbol{X}) = \beta + Z(\boldsymbol{X}) \tag{17}$$

where β is a hyperparameter which is the determined part and $Z(\boldsymbol{X})$ is a Gaussian stochastic process with zero mean and covariance in the form of

$$\mathrm{Cov}(Z(\boldsymbol{X}^{(i)}), Z(\boldsymbol{X}^{(j)})) = \sigma_z^2 R(\boldsymbol{X}^{(i)}, \boldsymbol{X}^{(j)}) \tag{18}$$

where R is the correlation function between two input points, and σ_z^2 the Gaussian process variance. For R, most applications use Gaussian function

$$R(\boldsymbol{X}^{(i)}, \boldsymbol{X}^{(j)}) = \exp(-d(\boldsymbol{X}^{(i)}, \boldsymbol{X}^{(j)})) \tag{19}$$

where $d(\boldsymbol{X}^{(i)}, \boldsymbol{X}^{(j)})$ is the distance function between $\boldsymbol{X}^{(i)}$ and $\boldsymbol{X}^{(j)}$. Usually it is a weighted distance function

$$d(\boldsymbol{X}^{(i)}, \boldsymbol{X}^{(j)}) = \sum_{k=1}^{z}\theta_k\left|x_k^{(i)} - x_k^{(j)}\right|^2 \tag{20}$$

Hyperparameters θ_k control the degree of nonlinearity in kriging surrogate model. Once they are found out, the prediction model would be built. Through maximum likelihood prediction, finding these hyperparameters transforms into solving a constrained minimization problem:

$$\begin{cases} \mathrm{Min}\varphi(\boldsymbol{\theta}) = |\boldsymbol{R}(\boldsymbol{\theta})|^{1/z}\sigma_z^2(\boldsymbol{\theta}) \\ \boldsymbol{\theta} = [\theta_1, \theta_2, \cdots, \theta_z]^{\mathrm{T}}, \ \ (\theta_j \ge 0)\big|_{j=1}^{z} \end{cases} \tag{21}$$

where $\boldsymbol{R}(\boldsymbol{\theta})$ is a $N \times N$ matrix whose ijth element is $\boldsymbol{R}(\boldsymbol{\theta})_{ij} = \boldsymbol{R}(\boldsymbol{X}^{(i)}, \boldsymbol{X}^{(j)})$, $\boldsymbol{I}$ is the unit matrix, and $\sigma_z^2(\boldsymbol{\theta})$ can be found out from

$$\begin{cases} \sigma_z^2 = \frac{1}{N}(\boldsymbol{Y} - \boldsymbol{I}\hat{\beta})^{\mathrm{T}}\boldsymbol{R}(\boldsymbol{\theta})^{-1}(\boldsymbol{Y} - \boldsymbol{I}\hat{\beta}) \\ \hat{\beta} = \frac{\boldsymbol{I}^{\mathrm{T}}\boldsymbol{R}(\boldsymbol{\theta})^{-1}\boldsymbol{Y}}{\boldsymbol{I}^{\mathrm{T}}\boldsymbol{R}(\boldsymbol{\theta})^{-1}\boldsymbol{I}} \end{cases} \tag{22}$$

Many methods could be used to solve the problem above, and in our study, genetic algorithm (GA) is adopted. Once the hyperparameters are known, the prediction model could be built in detail as

$$y(\boldsymbol{X}) = \hat{\beta} + \boldsymbol{r}^{\mathrm{T}}(\boldsymbol{X})\boldsymbol{R}(\boldsymbol{\theta})^{-1}(\boldsymbol{Y} - \boldsymbol{I}\hat{\beta}) \tag{23}$$

Here $\boldsymbol{r}(\boldsymbol{X}) = \left[R(\boldsymbol{X}, \boldsymbol{X}^{(1)}), R(\boldsymbol{X}, \boldsymbol{X}^{(2)}), \cdots, R(\boldsymbol{X}, \boldsymbol{X}^{(N)})\right]^{\mathrm{T}}$.

The prediction standard deviation is

$$\sigma = \sqrt{\sigma_z^2(1 - \boldsymbol{r}^{\mathrm{T}}(\boldsymbol{X})\boldsymbol{R}(\boldsymbol{\theta})^{-1}\boldsymbol{r}(\boldsymbol{X}))} \tag{24}$$

4. Flow field prediction based on POD and kriging surrogate model

In this section, the kriging surrogate model, instead of projection method, is used to find the coefficients of selected basis modes in Eq. (16). And the inner product forms for variable physical domain are discussed.

4.1. Combination of POD and kriging surrogate model

The principle that use kirging surrogate model to find basis modes coefficients out is: assume that that the flow field varies with the changing of z parameters $\boldsymbol{X} = [x_1, x_2, \cdots, x_z]^{\mathrm{T}}$ which could be, for example, the geometry parameters of the configuration. Let $\{\boldsymbol{U}^{(i)}\}_{i=1}^{N}$ be a set of snapshots corresponding to the parameter set $\{\boldsymbol{X}^{(i)}\}_{i=1}^{N}$. Do the POD process on the snapshots set and select the first P basis modes to approximate each snapshot following Eq. (13). Then a basis mode coefficients set $\{\boldsymbol{b}^{(i)}\}_{i=1}^{N}$ with $\boldsymbol{b}^{(i)} = [b_1^{(i)}, b_2^{(i)}, \ldots, b_P^{(i)}]^{\mathrm{T}}$ could be generated. That means the flow field $\boldsymbol{U}^{(i)}$ which is decided by $\boldsymbol{X}^{(i)}$ could be described by $\boldsymbol{b}^{(i)}$ approximately. So there is a certain function relationship $\boldsymbol{b} = F(\boldsymbol{X})$ between the parameters vector $\boldsymbol{X}$ and the coefficients vector $\boldsymbol{b}$. And, we can use kriging surrogate model to approximate this function relationship as $\boldsymbol{b} = F(\boldsymbol{X}) \approx \widehat{F}(\boldsymbol{X})$.

Since kriging surrogate model can just approximate the function relationship about single output variable, if the first P basis modes are selected to predict the flow field decided by any new parameters vector $\boldsymbol{b}$, then P kriging surrogate models should be built. Namely, for the coefficient of the jth basis mode, the function relationship $b_j \approx \hat{f}_j(\boldsymbol{X})$ should be constructed based on the database $\{b_j^{(i)}\}_{i=1}^{n}$ and $\{\boldsymbol{X}^{(i)}\}_{i=1}^{n}$. Finally, the basis mode coefficients for any new flow field $\boldsymbol{U}^{(\boldsymbol{X})}$ decided by parameters vector $\boldsymbol{X}$ are solved by

$$\begin{cases} b_1 \approx \hat{f}_1(\boldsymbol{X}) \\ b_2 \approx \hat{f}_2(\boldsymbol{X}) \\ \vdots \qquad \vdots \\ b_P \approx \hat{f}_P(\boldsymbol{X}) \end{cases} \tag{25}$$

Then, $\boldsymbol{U}^{(\boldsymbol{X})}$ could be approximated by Eq. (13) using these coefficients, namely

$$\boldsymbol{U}^{(\boldsymbol{X})} \approx \sum_{j=1}^{P} b^{(j)}\boldsymbol{\Phi}^{(j)}(x) + \overline{\boldsymbol{U}}(x) \tag{26}$$

From the process above, we do not introduce any assumption or constraint to the problem. The flow field prediction method is independent with the governing equations. So, compressibility and viscosity would not cause any trouble. And it is easy to extend this method to predict other physical fields or large-scale output problems.

4.2. Algorithm used to determine the number of modes

As mentioned in Section 2, the number of modes that should be used can be determined by the famous 99% energy criterion. Usually this criterion can promise a predicted result which is not very poor, but probably not the best one (as demonstrated in next section). For the prediction method used in this paper, a more applicable modes number could be determined during the prediction process. That is based on such a feature: if $\boldsymbol{U}_P^{(\boldsymbol{X})}$ is the predicted result of $\boldsymbol{U}^{(\boldsymbol{X})}$ by using the first P basis modes, then when we use the fist $P+1$ basis modes to repeat the prediction, we just need to build the kriging surrogate model for the $P+1$ basis mode. The new prediction result can be represented as

$$\boldsymbol{U}_{P+1}^{(\boldsymbol{X})} = \boldsymbol{U}_P^{(\boldsymbol{X})} + b_{P+1}\boldsymbol{\Phi}^{(P+1)}(x) \tag{27}$$

Based on the formula above, we can construct an efficient algorithm which can promise a good prediction result without trying all choices of modes number. Let q be an integer, d_P be the residual between $\boldsymbol{U}_{(P-1)}^{(\boldsymbol{X})}$ and $\boldsymbol{U}_{(P)}^{(\boldsymbol{X})}$, ε is the residual tolerance, and $\boldsymbol{U}_{(0)}^{(\boldsymbol{X})} = \overline{\boldsymbol{U}}(x)$. Then the procedure can be summarized as follows, beginning with $P = 1$.

Step 1. Build the surrogate model to predict the superposition coefficient b_P of the P th basis mode.
Step 2. Get $\boldsymbol{U}_P^{(\boldsymbol{X})}$ by using linear superposition between $\boldsymbol{U}_{(P-1)}^{(\boldsymbol{X})}$ and $\boldsymbol{\Phi}^{(P)}(x)$, namely Eq. (27). Then calculate d_P.
Step 3. If $P < q$, go to Step 5. Else, find out the maximum and minimum of data set $\{d_P, d_{P-1}, \ldots, d_{P-q+1}\}$, and name them $d_{\max}$ and $d_{\min}$ respectively.
Step 4. If $|d_{\max} - d_{\min}| \le \varepsilon$, then stop the iteration, the final modes number is P and the final prediction result is $\boldsymbol{U}_P^{(\boldsymbol{X})}$. Otherwise, go to Step 5.
Step 5. Set $P = P + 1$ and go to Step 1.

There are many choices about the criteria that used to quantify d_P in preceding iteration. In the present work, the difference between both surface pressure distributions (SPDs) which are extracted from both predicted flow fields is adopted. The definition is

$$d_P = \sqrt{\frac{1}{S}\sum_{i=1}^{S}\left(C_{pP+1}^{(i)} - C_{pP}^{(i)}\right)^2} \tag{28}$$

where $C_{pP+1}^{(i)}$ and $C_{pP}^{(i)}$ are the surface pressure coefficients of $\boldsymbol{U}_{(P+1)}^{(\boldsymbol{X})}$ and $\boldsymbol{U}_{(P)}^{(\boldsymbol{X})}$ at the ith grid vertex of all S grid vertexes that around the solid surface.

4.3. Inner product for variable physical domain

Usually, the inner product used in POD process about aerodynamic problem is defined on SIS. For example, the inner product between $\tilde{\boldsymbol{U}}^{(m)}$ and $\tilde{\boldsymbol{U}}^{(n)}$ from the snapshots set $\left\{\tilde{\boldsymbol{U}}^{(k)}(x) : 1 \le k \le N, x \in \Omega\right\}$ is

$$\left(\tilde{\boldsymbol{U}}^{(m)}, \tilde{\boldsymbol{U}}^{(n)}\right) = \int_{\Omega} \tilde{\boldsymbol{U}}^{(m)}\tilde{\boldsymbol{U}}^{(n)}\mathrm{d}\Omega = \int_{\Omega}\sum_{z=1}^{w}\tilde{U}_z^{(m)}\tilde{U}_z^{(n)}\mathrm{d}\Omega \tag{29}$$

where $\tilde{U}_z^{(m)}$ and $\tilde{U}_z^{(n)}$ are the zth variables of all w variables in $\tilde{\boldsymbol{U}}^{(m)}$ and $\tilde{\boldsymbol{U}}^{(n)}$ respectively. The last term of the equation above means the physical domain should be included in the inner

product in some certain forms. While, for the problem treated in this paper, the physical domains of flow fields are different from each other. It makes the operation of Eq. (29) hard to go on. Bourguet et al.[17] used Hadamard formulation to treat problem of flow field prediction around an airfoil submitted to small deformations. This approach captures airfoil profile deformations by a boundary conditions modification whereas the spatial domain remains unchanged. While using this method, you have to change your CFD code to solve the so-called HF Navier–Stokes equations. And the airfoil deformations in ROM are represented in some complex forms. Moreover, the deformations are constrained "small".

Actually, if all the snapshots are generated from the computations done on structured meshes which have the same topology and index, another simpler approach proposed by LeGresley and Alonso[19] could be applied. For the physical domain discretized by structured meshes, the discrete equivalent of the inner product in Eq. (29) is then

$$(\tilde{\boldsymbol{U}}^{(m)}, \tilde{\boldsymbol{U}}^{(n)}) = \sum_{i,j}\sum_{z=1}^{w} \tilde{U}_z^{(m)} \tilde{U}_z^{(n)} A_{ij} \tag{30}$$

where A_{ij} is the ensemble average area of the ijth grid cells in all snapshots measured in the physical domain. In this case, the domain is the same for all snapshots. Eq. (30) seems calculationally easy, but the area of the ijth grid cell in each snapshot should be solved out. Moreover, if the CFD code, which is used to calculate the snapshots, uses vertex scheme instead of cell-centered scheme, values of $\tilde{U}_z^{(m)}$ and $\tilde{U}_z^{(n)}$ at the center of the ijth cells should be predicted out from their values at the vertexes around the cells. If we need not to build a POD-Projection ROM system, just as what is being done in this paper, the physical domain needs not to be included into the inner product. So, it leads to the simplified inner product

$$(\tilde{\boldsymbol{U}}^{(m)}, \tilde{\boldsymbol{U}}^{(n)}) = \sum_{i,j}\sum_{z=1}^{w} \tilde{U}_z^{(m)} \tilde{U}_z^{(n)} \tag{31}$$

Compared with Eq. (30), it seems that the equation here just ignores the cell area item, and actually it convents the computation a lot. In Eq. (31), $\tilde{U}_z^{(m)}$ and $\tilde{U}_z^{(n)}$ could be their values either at the ijth grid vertexes or the center of the ijth grid cells, and it just depends on the scheme of the CFD code. Obviously, this simplified inner product turns to be the most common one defined on euclidean space (ES). It is more convenient and has higher computational efficiency. Moreover, it just requires that the meshes for both sets have the same topology and index. As for the physical domains, they can be different from each other.

5. Stationary flow fields prediction of different airfoils

In this section, we present the prediction results of stationary flow fields of different airfoils. In detail, we set $q = 4$ and $\varepsilon = 1.0 \times 10^{-6}$ as the iteration stop criteria. For comparison, all the prediction work is repeated with using two different inner product forms, namely, Eqs. (30) and (31). In the following sections, results signed by "SIS" means they are generated by using inner product in the form of Eq. (30), signed by "ES" means they are generated by using inner product in the form of Eq. (31), signed by "CFD" means they are generated by the CFD code directly.

The airfoils of the snapshots are generated by adding six hicks-henna bumps[26] and one CST classic function bump[27] onto both sides of the baseline airfoil RAE-2822. The CST bumps on both sides are used to change the slope at the trailing edge. The formula for hicks-henna bump is Eq. (32), for CST bump is Eq. (33).

$$y(x) = a\sin(\pi x^{\ln 0.5/\ln t}) \tag{32}$$

$$y(x) = a\frac{11!x^{10}(1-x)}{10!} \tag{33}$$

where t is the peak location of the hicks-henna bump; the peak locations of the six hicks-henna bumps are $0.1c$ $0.25c$ $0.45c$ $0.65c$ $0.8c$ and $0.9c$, c is the chord length of the baseline airfoil; a is the coefficient of the bump height which is generated by Latin hypercube sample method.[28] For the first four hicks-henna bumps, the height coefficient intervals are [0.004, 0.004], for the 5th, 6th and the CST bumps are [0.002, 0.002], [0.001, 0.001] and [0.001, 0.001] respectively.

Two hundred airfoils are generated to compute their stationary flow fields as snapshots. The CFD code solves Reynolds averaged Navier–Stokes equations using vertex scheme. The trailing edges of all airfoils are sharp, and the mesh type is typical C mesh with 320×64 cells. Ten airfoils beyond the snapshots are generated as testing samples. The prediction is repeated under two different conditions. The first is totally subsonic condition with freestream Mach number $Ma = 0.50$, Reynolds number $Re = 4.0 \times 10^6$ and angle of attack $\alpha = 2.8°$. The second is transonic conditions with freestream $Ma = 0.72$, $Re = 5.4 \times 10^6$ and $\alpha = 2.8°$.

Fig. 1(a) shows the baseline airfoil RAE-2822, the thickest and thinnest airfoils that could be generated from the intervals of all bump height coefficients. Their corresponding SPDs under both testing conditions are shown in Fig. 1(b) and Fig. 1(c). From both figures, under subsonic condition, the negative pressure peak of SPD at the leading edge on upper surface changes

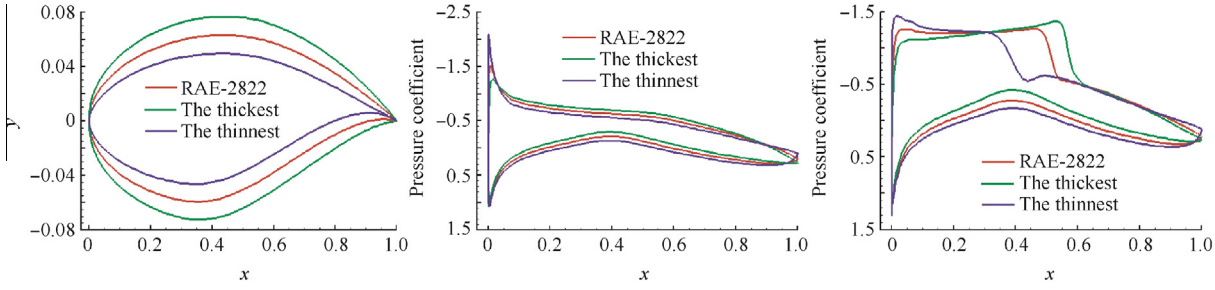

(a) Baseline airfoil (b) Corresponding SPDs under Ma=0.5 (c) Corresponding SPDs under Ma=0.72

Fig. 1 Profiles of baseline airfoil, the probable thickest and the thinnest snapshot airfoil.

much drastically than other segments. While, variation of the shock wave under the transonic condition is the most attractive part. Generally, variation range of the SPD caused by the airfoil profile changing is wider under Mach number 0.72.

The variables u, v, Ma, and C_p are considered to be predicted in the flow fields of the ten testing airfoils, where u and v are the velocity along x and y directions, and C_p is the pressure coefficient. Since it is hard to define an error measure criterion which could consider all the four variables at the same time, the error of the predicted SPDs is used to represent the prediction precision indirectly. The definition is similar with Eq. (28), namely

$$E = \sqrt{\frac{1}{S}\sum_{i=1}^{S}(C_{pe}^{(i)} - C_p^{(i)})^2} \tag{34}$$

where $C_{pe}^{(i)}$ and $C_p^{(i)}$ are the predicted pressure coefficient and the value solved by the CFD code at the ith grid vertex of all S grid vertexes that around the airfoil surface.

5.1. Results for Mach number 0.50

The energy curves of both basis mode sets generated by using both forms of inner product and the average flow field are presented in Fig. 2. The average flow field is generated by assigning the average values of each flow field variable at each grid node to the corresponding grid node of the average mesh of all snapshots. For the criterion of 99% energy, just the first 6 basis modes, which contain 99.056% energy in total, could satisfy it. And the first 12 modes that contain 99.224% energy in total are needed corresponding to the ES result. It seems

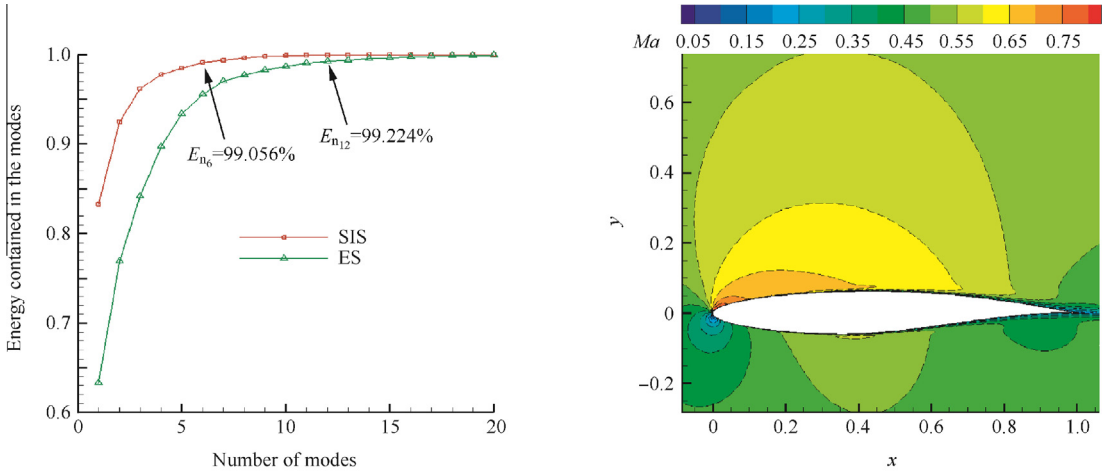

(a) Average flow field of all 200 snapshots (b) Ma=0.5

Fig. 2 Energy curves generated using both inner product definitions.

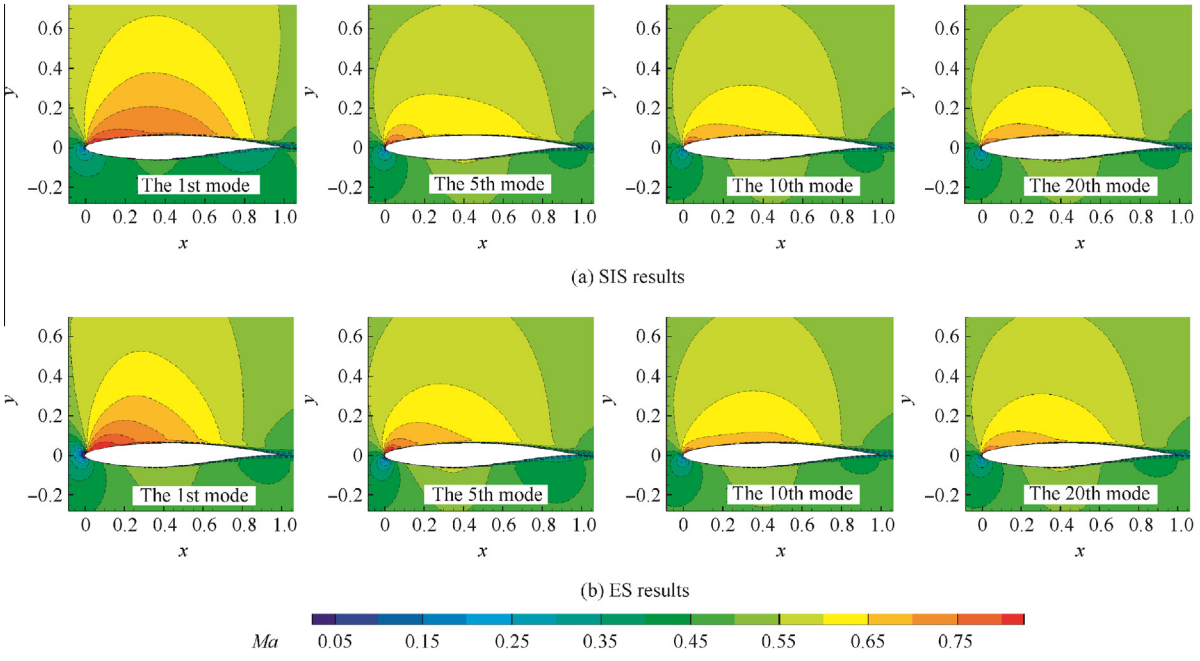

Fig. 3 Flow fields of selected basis modes in case Ma = 0.5.

that it is easier to concentrate the energy into the modes ranking front when using the inner product defined on SIS.

Fig. 3 shows the 1st, 5th, 10th and 20th basis modes generated using both forms of inner product (actually, they are the flow fields of $\boldsymbol{\Phi} + \overline{\boldsymbol{U}}$). Compared with the average flow field, the variation happening near the leading edge on the upper surface is the most obvious in these basis modes. That means the most significant variation characters among all the snapshots are around here. The 10th SIS basis mode is close to the average flow field already, while, the corresponding ES one still has obvious difference compared with the average flow field. This phenomenon fits with the difference between their corresponding energy curves in Fig. 2.

The boxplots of prediction errors defined by Eq. (34) of the 10 testing airfoils are presented in Fig. 4. In general, the error converges when the first 18 modes are used when using the SIS inner product, the corresponding number is 13 for using ES inner product. Moreover, the general prediction precision is higher with using SIS inner product after the prediction error is converged.

In detail, the prediction process and results of the 3rd and 4th testing flow fields are given here. As shown in Fig. 5, if using the iteration algorithm proposed in this paper to predict both testing flow fields, the modes number is 29 (SIS) and 35 (ES) respectively. If using the 99% energy criterion, for both testing flow fields, the modes number is 6 (SIS) and 12 (ES) respectively, just as signed in Fig. 2(a). The prediction errors of both testing flow fields are presented in Fig. 6. Generally, when the inner product is defined on SIS, using the modes number determined by the 99% energy criterion, the prediction error is much higher than the converged error value. In contrast, the iteration algorithm could provide a proper result which attaches the converged error value with no redundant basis modes. By using the inner product defined on ES, both criteria provide the results at the same precision level, but more redundant basis modes are used in the iteration algorithm.

When the first 30 basis modes are used, the predicted SPDs and SPDs $\pm\sigma$ of the 3rd and 4th testing airfoils are presented in Fig. 7. From this figure, both SPDs are predicted precisely, though both predicted SPDs of the 4th testing airfoil deviate

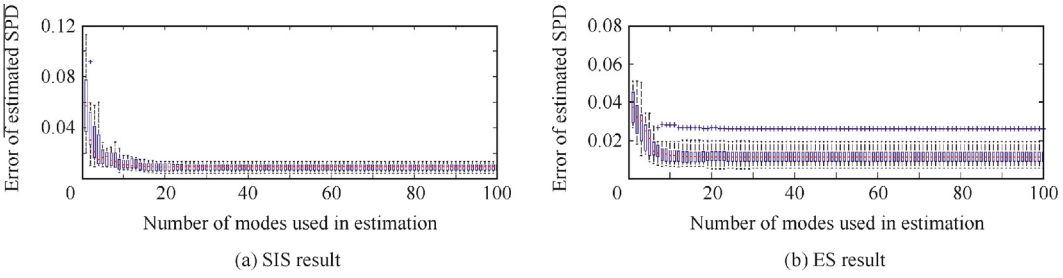

Fig. 4 Boxplots about prediction errors of SPDs of the ten testing airfoils in case of $Ma = 0.5$.

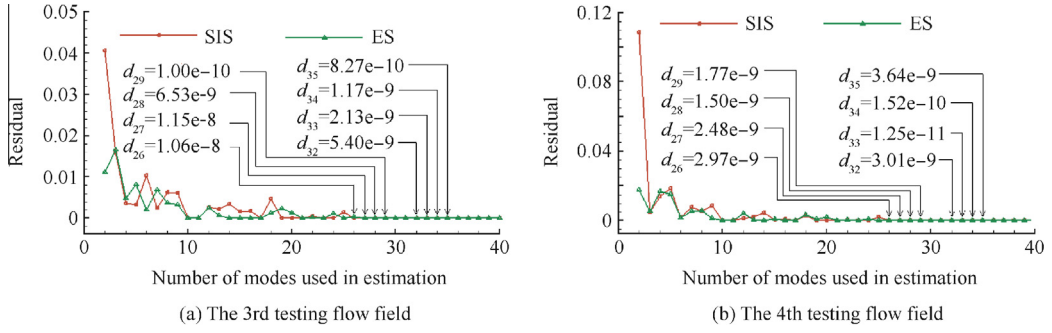

Fig. 5 Residual convergence process of testing flow fields in case of $Ma = 0.5$.

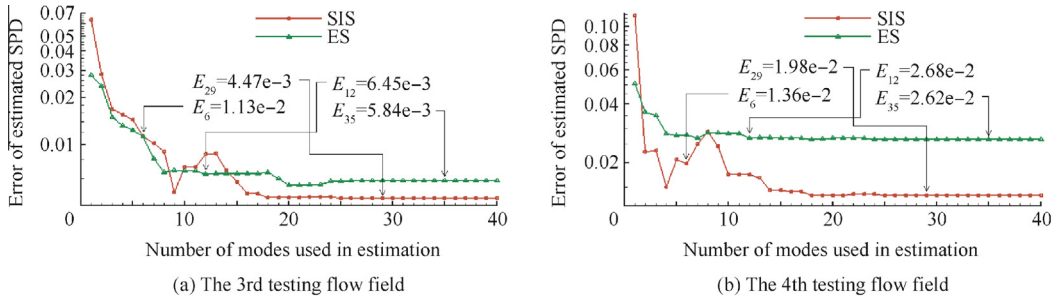

Fig. 6 Prediction error vs modes number of testing flow fields in case of $Ma = 0.5$.

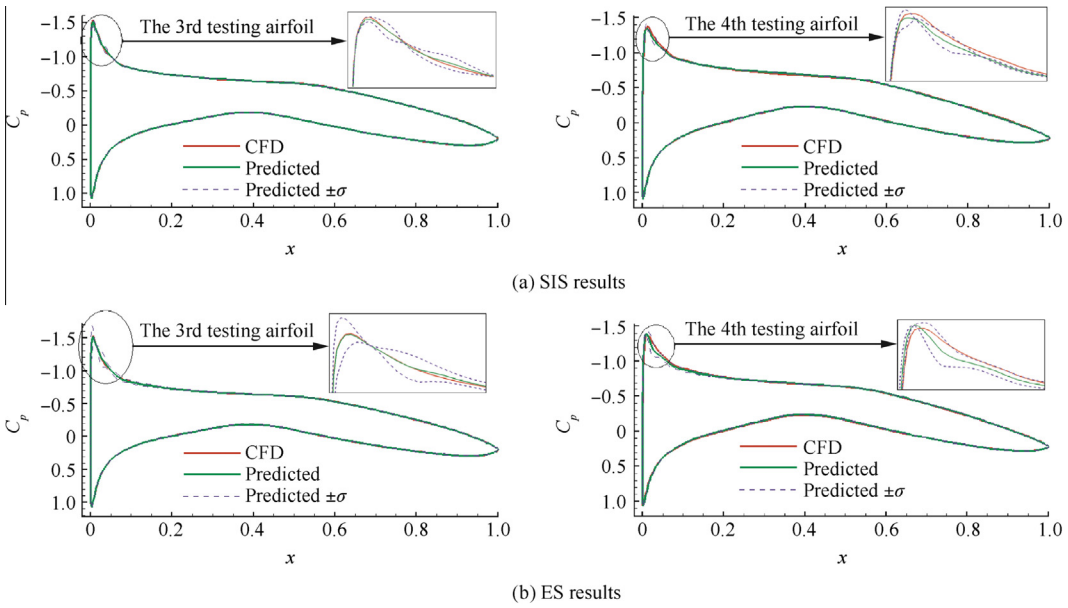

Fig. 7 Predicted SPDs and errors ($\pm\sigma$) of the testing airfoil using the first 30 modes in the case of $Ma = 0.5$.

from the CFD one a little at the negative peak segment. Similarly, for both testing airfoils, the predicted velocity profiles (see Fig. 8) near trailing edge on upper surface, where the boundary layer is the thickest, have good agreements with the CFD ones using both forms of inner products. Fig. 9 shows the predicted Mach number contours of both testing flow fields. Both SIS results and ES result of the 3rd testing flow field nearly cover the corresponding CFD result. While, similar to the predicted SPD, ES result of the 4th testing flow field biases the CFD results a little.

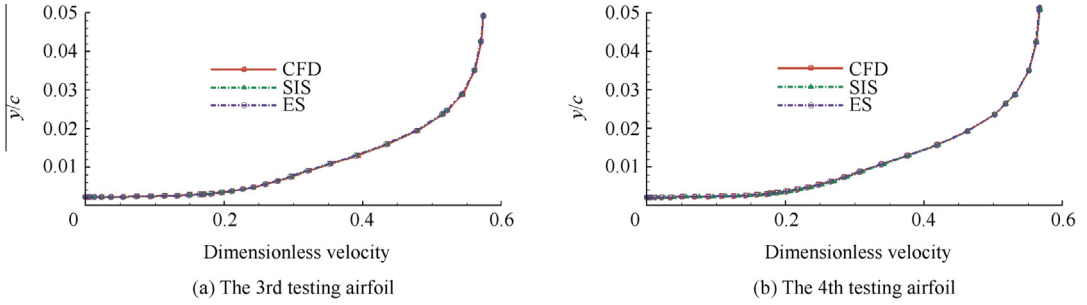

Fig. 8 Predicted velocity profiles at $x/c = 0.99$ on upper surface of two testing airfoils when the first 30 modes are used in the case of $Ma = 0.5$.

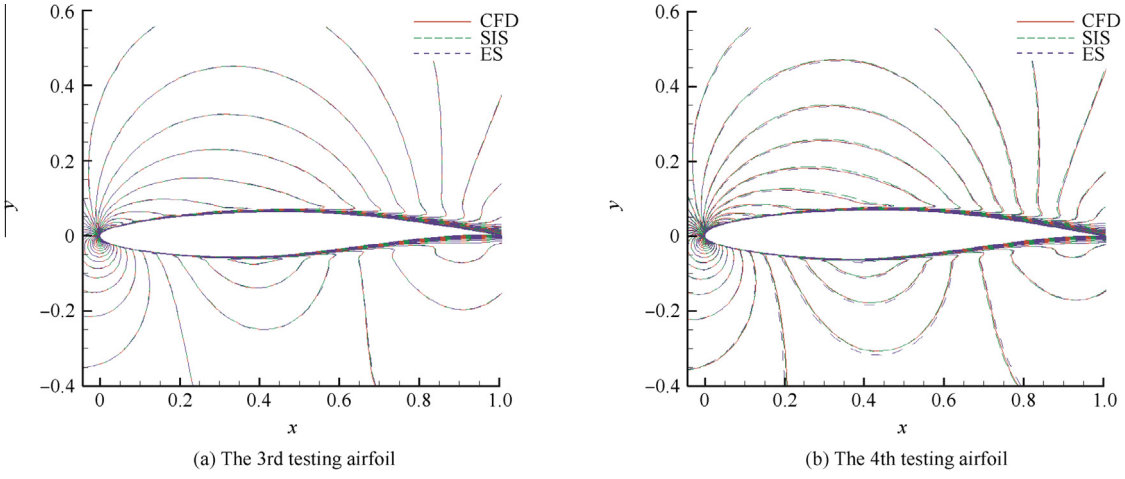

Fig. 9 Predicted Mach number contours of two testing airfoils when the first 30 modes are used in the case of $Ma = 0.5$.

5.2. Results for Mach number 0.72

When the flow condition changes to Mach number 0.72, with either inner product form, the energy contained in the modes ranking front is less than that in case Mach number 0.5, just as indicated in Fig. 10. For satisfying the 99% energy criteria, the first 12 and 15 modes are needed using SIS and ES inner product respectively. We can speculate that the variation characters contained in the snapshots are more complex than that in case Mach number 0.5. Fig. 11 shows the flow fields of the 1st, 5th, 10th and 20th basis modes generated using both forms of inner product. Compared with the average flow field presented in Fig. 10(b), the most obvious difference exists in these modes are the intensity and amount of discontinuous stripes. From this figure, the number of discontinuities increases with the increase of mode number, while their intensity decreases. This phenomenon can be explained as follows: most characteristics of shock waves of different intensities at different positions contained in all the snapshots have been decomposed into the modes ranked in front. As the results presented in the following paragraphs, this kind of discontinuities distribution in the modes causes some trouble for the shock wave prediction.

The boxplots presented in Fig. 12 indicates that the general prediction precision decreases a lot compared with the situation in case $Ma = 0.5$. The convergence modes number of the error is 36 for SIS result and 13 for ES result. Inverse to the situation in case $Ma = 0.5$, the general prediction precision using the ES inner product is slightly better than that with the SIS inner product.

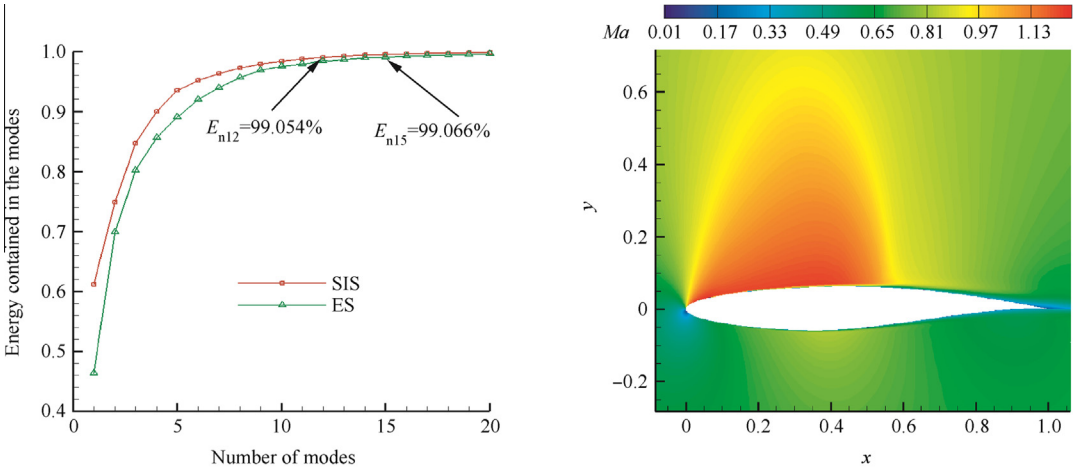

(a) Average flow field of all 50 snapshots (b) In the case of Ma=0.72

Fig. 10 Energy curves generated with using both inner product definitions.

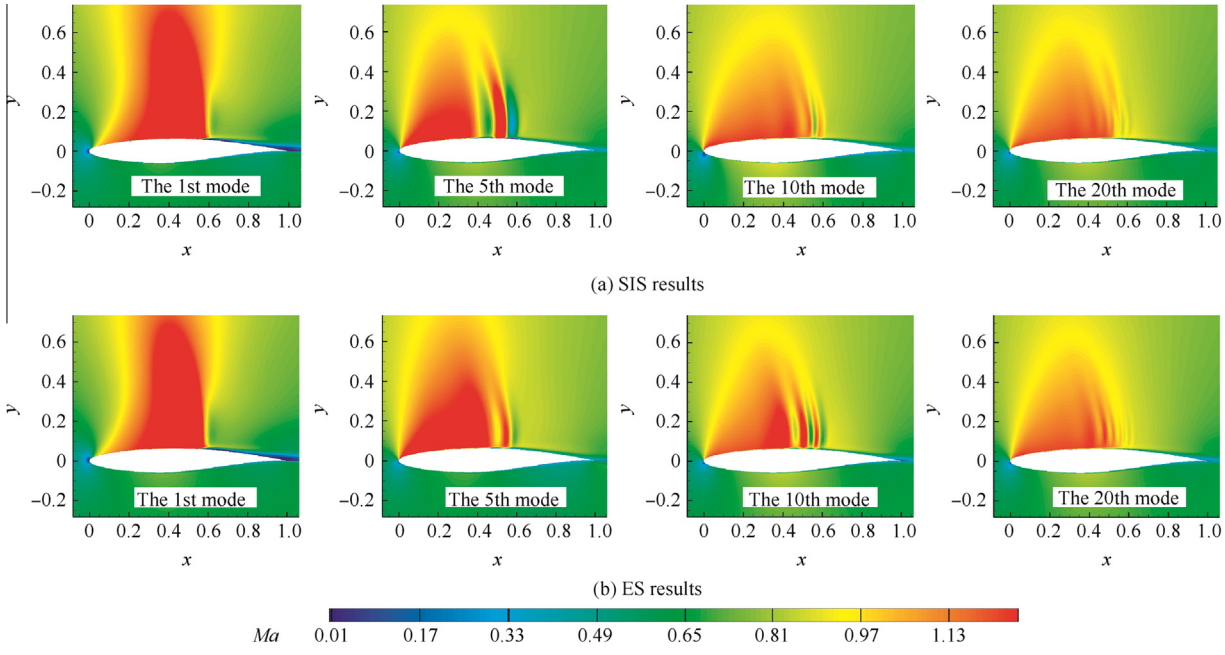

Fig. 11 Flow fields of selected modes in the case of $Ma = 0.72$.

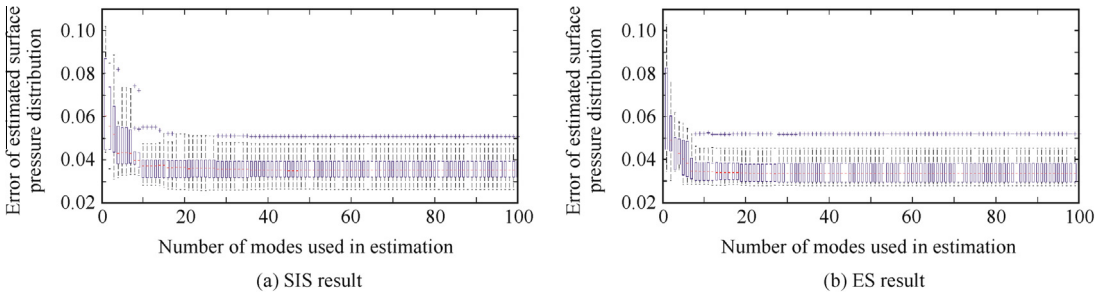

Fig. 12 Boxplots about prediction errors of SPDs of the 10 testing airfoils in the case of $Ma = 0.72$.

In detail, the prediction process and results of the 2nd and 4th testing flow fields are researched carefully. As shown in Fig. 13, if using the iteration algorithm proposed in this paper to predict the 2nd testing flow field, the modes number is 32 (SIS) and 25 (ES); to predict the 4th testing flow field, the modes number is also 32 (SIS) and 25 (ES). If using the 99% energy criterion, for both testing flow fields, the modes number is 12 (SIS) and 15 (ES) respectively, just as signed in Fig. 10(a). As shown in Fig. 14, if the inner product is defined on SIS, the 99% energy criterion fails to determine a proper modes number where the error has been converged. But if the inner product is defined on ES, then this criterion determines precisely. While, no matter which inner product is used, the numbers of modes determined by the iteration algorithm exceed the optimal numbers significantly for both testing airfoils.

The predicted SPDs and SPDs $\pm\sigma$ of the 2nd and 4th testing airfoils by using the first 30 modes are presented in Fig. 15. Clearly, the main part of the prediction error here comes from the poorly predicted shock waves. From this figure, the prediction standard deviations of SPD at the segments around the shock waves are much bigger than that at other segments, and all the predicted SPDs deviate from the CFD ones obviously in the same area. But all the predicted results have good agreement with the CFD ones on the lower surface and the back segment of upper surface. Moreover, compared with the CFD results, all the predicted shock waves are wider and less distinct. This phenomenon is much more obvious in Fig. 16, where the predicted shock waves are fuzzier than the CFD ones, especially for the 4th testing flow fields. Even, a noise stripe, as indicated by the black arrows, occurs in both predicted results of the 2nd testing flow field. This noise stripe does not exist in the CFD flow field, and it is very distinct in the ES result. In Fig. 17, the velocity profiles, at $x/c = 0.99$ on the upper surface extracted from predicted flow fields, coincide with the CFD ones very well for the 2nd testing flow field. Though for the 4th testing airfoil, they slightly deviate from the CFD ones, while, they have similar profiles to the CFD ones.

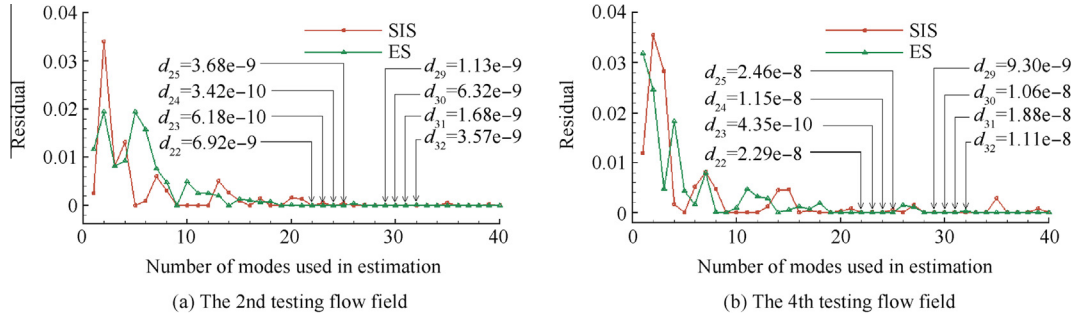

Fig. 13 Residual convergence process of two testing flow fields in the case of $Ma = 0.72$.

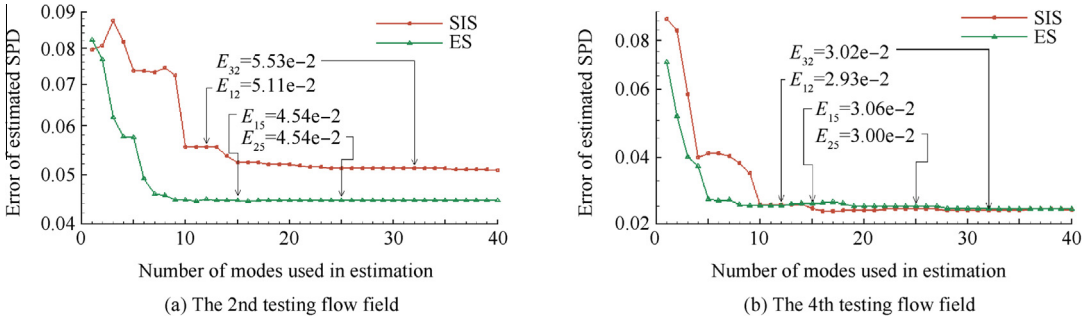

Fig. 14 Prediction error vs modes number of two testing flow fields in the case of $Ma = 0.72$.

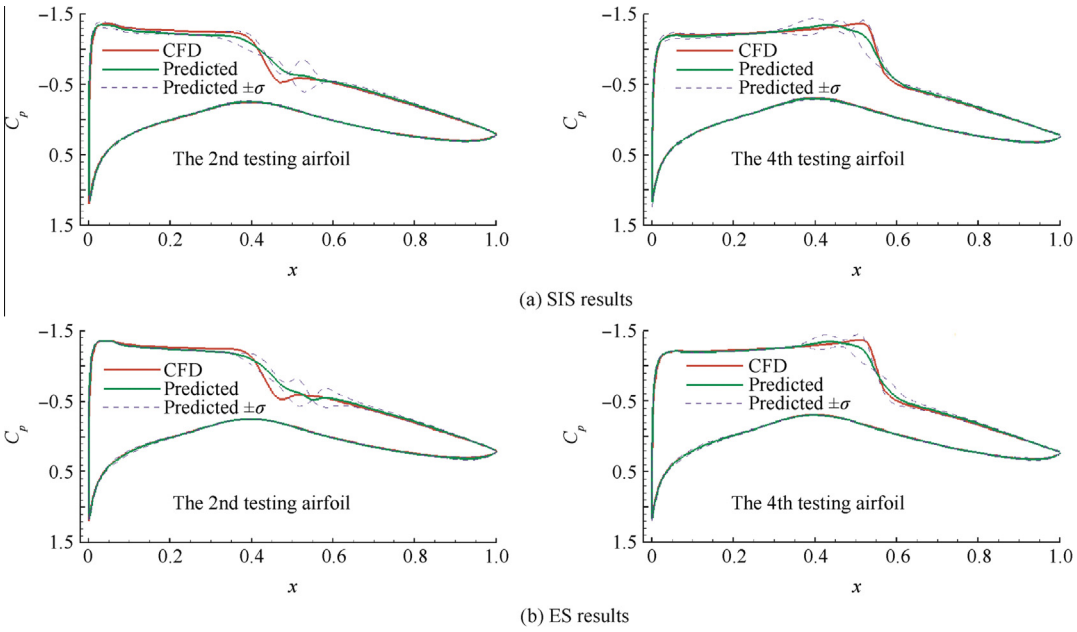

Fig. 15 Predicted SPDs and errors ($\pm\sigma$) of two testing airfoil with the first 30 modes in the case of $Ma = 0.72$.

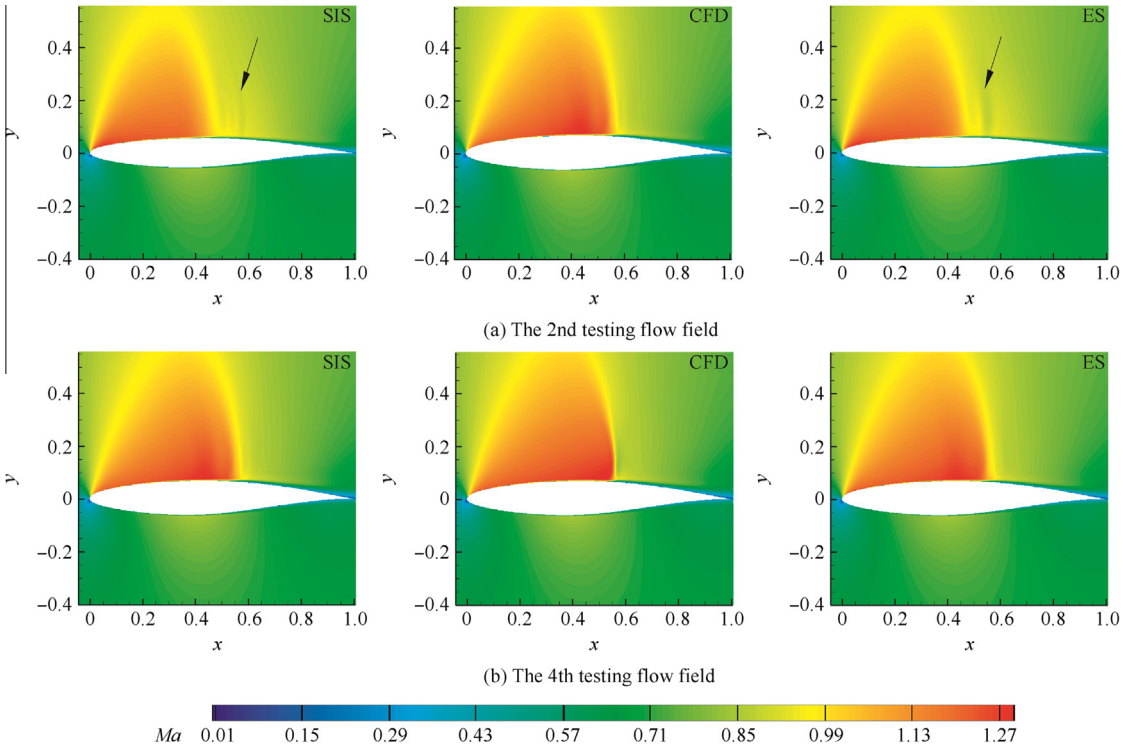

Fig. 16 Predicted Mach number cloud pictures of two testing airfoils when the first 30 modes are used in the case of $Ma = 0.72$.

5.3. Analysis of prediction results of flow fields containing shock waves

From the results presented in both sections above, the prediction precision in case $Ma = 0.72$ decreases more than that that in case $Ma = 0.5$. Naturally, on the one hand, this is caused by the wider variation range of the snapshots in the transonic case. On the other hand, the characteristic of the transonic basis modes should also be in charge of the decrement of the prediction precision.

As shown in Fig. 11, there are more than one discontinuous strips in the flow fields of these modes ranking front. Obviously, this is caused by the POD process which concentrates most shock wave discontinuities contained in snapshots into these modes. Each predicted flow field is generated from the linear superposition of these modes, namely Eq. (16). So,

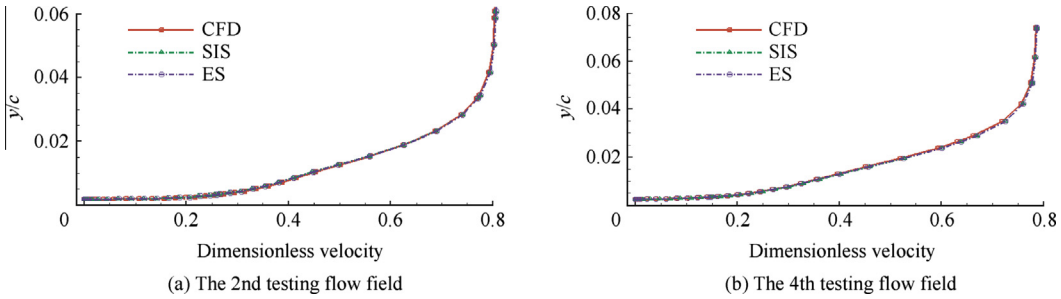

(a) The 2nd testing flow field (b) The 4th testing flow field

Fig. 17 Predicted velocity profiles at $x/c = 0.99$ on upper surface of two testing airfoils when the first 30 modes are used in the case of $Ma = 0.72$.

shock waves contained in the predicted flow fields come from the linear superposition of these discontinuous stripes contained in selected modes. Probably, the superposition of these discontinuous stripes, which are located near the exact shock wave position, could generate the desired approximate shock wave, but these remaining discontinuities could not cancel mutually. Then those noise stripes appear. And, since each discontinuous stripe is much wider than exact shock waves, the predicted shock waves are also wider and fuzzier.

Since both the position and strength of the shock wave are very important features in a transonic or supersonic flow field, the method developed in this paper is not proper for flow field containing shock wave.

6. Conclusions

(1) A flow field prediction method based on Kriging surrogate model and POD is developed to predict stationary flow fields of variable physical domain. Two forms of inner product are constructed to figure out the variable physical domain problem. An iterative algorithm is proposed to determine how many basis modes ranking front should be used in the prediction.

(2) Testing results of subsonic stationary flow fields around airfoils are very precise compared with CFD results. While under transonic condition, the prediction precision decreases a lot. Partially, it is caused by the larger variation range of snapshots. Mainly, it is caused by the inherent defect of linear superposition of discontinuous stripes contained in the main basis modes. So, the prediction method developed in this paper is very proper for the subsonic flow field, but not proper for the flow field contains shock wave.

(3) The testing results also indicate that the iteration algorithm could determine a proper modes number if both the stop criterion parameters are reasonable. But it is hard to give such reasonable parameters in prior. So, we suggest that it is better to set a relatively strict stop criterion which could promise a precision result.

Acknowledgements

The authors thank to Prof. P.B. Nair (University of Toronto Institute for Aerospace Studies) who introduced his helpful work. We also thank P. A. LeGresley (Stanford University Aerospace Computing Laboratory) who responded enthusiastically when we consulted him questions about inner product. This study was supported by the National Basic Research Program of China (No. 2014CB744804).

References

1. Holmes P, Lumley JL, Berkooz G. *Turbulence, coherent structures, dynamical systems and symmetry*. New York: Cambridge University Press; 1996. p. 86–113.
2. Sirovich L. Turbulence and the dynamics of coherent structures, parts I–III. *Q Appl Math* 1987;**45**(3):561–71.
3. Aubry N, Holmes P, Lumley JL, Stone E. The dynamics of coherent structures in the wall region of a turbulent boundary layer. *J Fluid Mech* 1988;**7**:115–73.
4. Lucia DJ, Beran PS. Projection methods for reduced order models of compressible flows. *J Comput Phys* 2003;**188**(1):252–80.
5. Hall KC, Thomas JP, Dowell EH. Proper orthogonal decomposition technique for unsteady transonic aerodynamic flows. *AIAA J* 2000;**38**(10):1853–62.
6. Anttonen JSR, King PI, Beran PS. Applications of multi-POD to a pitching and plunging airfoil. *Math Comput Modell* 2005;**42**(Suppl. 3):245–59.
7. Willcox K, Peraire J, Paduano J. Application of model order reduction to compressor aeroelastic models. *J Eng Gas Turbines Power* 2002;**124**(2):332–9.
8. Ma X, Karniadakis GE. A low-dimensional model for simulating three-dimensional cylinder flow. *J Fluid Mech* 2002;**5**:181–90.
9. Noack BR, Afanasiev K, Morzynski M, Tadmor G, Thiele F. A hierarchy of low-dimensional models for the transient and post-transient cylinder wake. *J Fluid Mech* 2003;**12**:335–63.
10. Galletti B, Bruneau CH, Zannetti L, Iollo A. Low-order modelling of laminar flow regimes past a confined square cylinder. *J Fluid Mech* 2004;**3**:161–70.
11. Noack B, Papas P, Monkewitz P. The need for a pressure-term representation in empirical Galerkin models of incompressible shear flows. *J Fluid Mech* 2005;**1**:339–65.
12. Buffoni M, Camarri S, Iollo A, Salvetti MV. Low-dimensional modeling of a confined three-dimensional wake flow. *J Fluid Mech* 2006;**12**:141–50.
13. Couplet M, Basdevant C, Sagaut P. Calibrated reduced-order POD-Galerkin system for fluid flow modeling. *J Comput Phys* 2005;**207**(1):192–220.
14. Ly HV, Tran HT. Proper orthogonal decomposition for flow calculations and optimal control in a horizontal CVD reactor. *Q Appl Math* 2002;**60**(4):631–56.
15. Zokagoa JM, Soulaïmani A. A POD-based reduced-order model for free surface shallow water flows over real bathymetries for Monte-Carlo-type applications. *Comput Meth Appl Mech Eng* 2012;**5**:1–23.
16. Rowley CW, Colonius T, Murray RM. Model reduction for compressible flows using POD and Galerkin projection. *Physica D* 2004;**189**(Suppl. 1):115–29.

17. Bourguet R, Braza M, Dervieux A. Reduced-order modeling of transonic flows around an airfoil submitted to small deformations. *J Comput Phys* 2011;**230**(1):159–84.
18. Anttonen JSR, King PI, Beran PS. POD-based reduced-order models with deforming grids. *Math Comput Modell* 2003;**38**(Suppl. 1): 41–62.
19. LeGresley PA, Alonso JJ. Investigation of non-linear projection for POD based reduced order models for aerodynamics. 2001. Report No.: AIAA-2001-0926.
20. Audouze C, Vuyst FD, Nair PB. Reduced-order modeling of parameterized PDEs using time-space-parameter principal component analysis. *Int J Numer Methods Eng* 2009;**80**(8):1025–57.
21. Bui-Thanh T, Willcox K, Damodaran M. Applications of proper orthogonal decomposition for inviscid transonic aerodynamics. 2003. Report No.: AIAA-2003-4213.
22. Qiu YS, Bai JQ, Hua J. Flow field estimation method based on proper orthogonal decomposition and surrogate model. *Acta Aeronaut Astronaut Sin* 2013;**34**(6):1249–60 Chinese.
23. Keane AJ, Nair PB. *Computational approaches for aerospace design the pursuit of excellence*. West Sussex: John Wiley & Sons Ltd.; 2005. p. 243–52.
24. Jolliffe I. *Principal component analysis*. 2nd ed. New York: Springer-Verlag; 2002. p. 10–29.
25. Kanwal RP. *Linear integral equations: theory and technique*. Boston: Birkhäuser; 1997. p. 125–56.
26. Hicks RM, Henne PA. Wing design by numerical optimization. 1977. Report No.: AIAA-1977-1247.
27. Kulfan BM, Bussoletti JE. Fundamental parametric geometry representations for airfoil component shapes. 2006. Report No.: AIAA-2006-6948.
28. Sacks J, Welch WJ, Michell TJ, Wynn HP. Design and analysis of computer experiments. *Stat Sci* 1989;**4**(4):409–35.

Qiu Yasong is a Ph.D. candidate at School of Aeronautics, Northwestern Polytechnical University, China. His main research interests are aerodynamic shape optimization and new reduce order method.

Bai Junqiang is a professor and Ph.D. supervisor at School of Aeronautics, Northwestern Polytechnical University, China. His main research interests are aircraft design, turbulence flow simulation and aeroelasticity simulation and control.